

# PST: Plant Segmentation Transformer Enhanced Phenotyping of MLS Oilseed Rape Point Cloud

Ruiming Du <sup>a, b</sup>, Zhihong Ma <sup>a, b</sup>, Pengyao Xie <sup>a, b</sup>, Haiyan Cen <sup>a, b\*</sup>, Yong He <sup>a, b\*</sup>

<sup>a</sup> *College of Biosystems Engineering and Food Science, State Key Laboratory of Modern Optical  
Instrumentation, Zhejiang University, Hangzhou 310058, P.R. China*

<sup>b</sup> *Key Laboratory of Spectroscopy Sensing, Ministry of Agriculture and Rural Affairs, Hangzhou 310058, P.R.  
China*

## **Abstract:**

Segmentation of plant point clouds to obtain high-precise morphological traits is essential for plant phenotyping and crop breeding. Although the bloom of deep learning methods has boosted much research on the segmentation of plant point cloud, most works follow the common practice of hard voxelization-based or down-sampling-based methods. They are limited to segmenting simple plant organs, overlooking the difficulties of resolving complex plant point clouds with high spatial resolution. In this study, we propose a deep learning network plant segmentation transformer (PST) to realize the semantic and instance segmentation of MLS (Mobile Laser Scanning) oilseed rape point cloud, which characterizes tiny siliques and dense points as the main traits targeted. PST is composed of: (i) a dynamic voxel feature encoder (DVFE) to aggregate per point features with raw spatial resolution; (ii) dual window sets attention block to capture the contextual information; (iii) a dense feature propagation module to obtain the final dense point feature map. The results

proved that PST and PST-PointGroup (PG) achieved state-of-the-art performance in semantic and instance segmentation tasks. For semantic segmentation, PST reached 93.96%, 97.29%, 96.52%, 96.88%, and 97.07% in mean IoU, mean Precision, mean Recall, mean F1-score, and overall accuracy, respectively. For instance segmentation, PST-PG reached 89.51%, 89.85%, 88.83% and 82.53% in mCov, mWCov, mPerc<sub>90</sub>, and mRec<sub>90</sub>, respectively. This study extends the phenotyping of oilseed rape in an end-to-end way and proves that the deep learning method has a great potential for understanding dense plant point clouds with complex morphological traits.

**Keywords:** 3D Deep learning; Point cloud segmentation; Mobile laser scanning; Plant phenotyping

## 1. Introduction

Plant morphological traits are essential in botanical and agricultural research, providing valuable information for plant breeding and harvest management (Tran et al., 2017). Oilseed rape, with superior nutritional quality, is regarded as one of the most important oil industrial crops and is cultivated worldwide (Friedt et al., 2007). The siliques are the main contributions to the seed yield of oilseed rape, the phenotypic traits of which are widely leveraged for yield estimation. Specifically, the growth locations (Oleksy et al., 2018), mature degree (Wang et al., 2016), total numbers, and length (Wolko et al., 2019) of the siliques are significantly related to the productivity and oil quality of oilseed rape. Traditional methods for phenotypic traits analysis rely on labor-

intensive and destructive manual measurement (Tanksley, 2004), while the development of image sensing and processing techniques provides high-throughput approaches. The prerequisite of these approaches to give reliable yield estimation lies in the precise segmentation of plant organs. However, the structure of the oilseed rape in the podding stage is complex, where plenty of tiny siliques scatter and overlap within a plant, making it difficult to recognize them. The high-precise segmentation of oilseed rape, therefore, still remains a challenge.

Among current high-throughput pipelines, the most widely used two-dimensional (2D) image-based approaches for plant organ segmentation are restricted by fluctuating illumination or organ overlap. (Li et al., 2020). While recent improvements in three-dimensional (3D) sensors and methods for understanding 3D data benefit much research tackling these problems. Accurate 3D data from various sensors, such as structured light, time-of-flight (TOF) cameras, and Laser scanners, preserves complete spatial information and enable quantitative assessment of different phenotype traits of the plant (Li et al., 2022; Ni et al., 2021; Xi et al., 2020), showing great potential in enabling the high-precise segmentation of oilseed rape. However, the measurement error for the current widely used TOF and structured light sensors varies from 1mm to centimeter-level due to numerous factors such as the wiggling effect or the measured distance (Fuersattel et al., 2017; Fursattel et al., 2016; Rauscher et al., 2016). The siliques have a slim shape with a much smaller relative width, requiring a high-resolution depicting. Thus, the 3D data of oilseed rape acquired by TOF or structured light sensors may be less precise and unreliable. Mobile laser scanning (MLS)

point cloud, one of the main forms of 3D data, is used to present detailed objects with high precision (Han et al., 2021), making it an ideal data source to enhance the phenotyping of oilseed rape with tiny scale traits. With such backing, we propose a fully annotated MLS oilseed rape point cloud dataset in this study for high-precise 3D phenotyping.

It is very challenging to segment MLS oilseed rape point clouds due to two main reasons: (i) MLS point clouds are of high density, making it hard to assign semantic labels for each point in a dense spatial resolution, and (ii) silique distributions are disordered with strong scattering and mutual overlapping in 3D space. Considering the data property of MLS point clouds and the complexity of the plant structure, a feasible segmentation pipeline is required to accurately detect and extract detailed traits of the oilseed rape without compromising data resolution.

Traditional methods investigate various 3D features defined by geometry properties and hand-crafted descriptions. They segment plant structures based on their 3D skeleton (Zermas et al., 2017), fast point feature histograms of the coordinate set (Sodhi et al., 2017; Wahabzada et al., 2015), or surface curvature and normals (Li et al., 2017; Li et al., 2013). 3D reconstruction, registration, and noise filtering strategies are widely used as prerequisites in these methods for subsequent processes (Dutagaci et al., 2020; Golbach et al., 2016; Ni et al., 2021). However, the traditional methods, including the prerequisites, rely highly on predefined rules and prior knowledge of the segmented targets. Given that segmentation quality is greatly influenced by the characteristics of different targets and parameter tuning (Vo et al., 2015), these methods are hence time and labor-consuming.

In addition, the limited prior knowledge of plant morphology constrains traditional methods of plant 3D phenotyping on simple structures and traits (Gibbs et al., 2020; Paulus et al., 2014; Xiang et al., 2019).

On the other hand, deep-learning-based methods for point cloud segmentation have recently emerged to tackle the above challenge. In contrast to leveraging prior knowledge, they learn features from input data in a data-driven manner. Benefit from the advanced neural networks, deep learning methods outperform most traditional methods, showing great potential in plant 3D phenotyping (Guo et al., 2020a). Current deep-learning-based methods on plant point clouds segmentation can be further divided into voxel-based and point-based methods (Guo et al., 2020b). Voxel-based methods transpose the point clouds into grids, and the regular voxel grids representation, like pixels in 2D images, can easily be analyzed by borrowing de-facto techniques from 2D counterparts, such as 3D convolution neural network (CNN) (Huang and You, 2016) and fully-convolutional point network (FCPN) (Rethage et al., 2018). Jin et al. (2020a) developed a voxel-based convolutional neural network VCNN to realize the classification and segmentation of maize at different growth stages. Though voxel-based can take in a dynamic number of input points, the traditional voxelization strategy, following the scheme of hard voxelization (HV) (Lang et al., 2019; Zhou et al., 2019; Zhou and Tuzel, 2018), may obscure the information of the raw inputs (Sec. 3.4). Besides, the paradigm of using convolution-based techniques on voxel grids is hard to balance the performance and computational cost. Point-based methods avoid obscuring invariances

of the original data by directly learning features of each point using shared multi-layer perceptron (MLP) (Engelmann et al., 2019; Qi et al., 2017a; Yang et al., 2019), point-wise convolution (Hua et al., 2018; Thomas et al., 2019; Xu et al., 2021), or recurrent neural network (RNN) (Engelmann et al., 2017; Huang et al., 2018; Ye et al., 2018). Li et al. (2022) proposed a dual-function point-based network PlantNet to realize semantic and instance segmentation of plant organs on three species. Jin et al. (2020b) proposed a point-based fully convolutional neural network PFCN to segment forest fields. Turgut et al. (2022) evaluated how the synthetic plant data affected the performance of existing point-based deep learning algorithms. However, for most point-based methods, the network architecture and hyper-parameters are mainly designed for small-scale inputs due to hardware limitations. Thus, the computation cost of point-based methods is highly sensitive to the number of input points, and a full-scale input will either increase the training speed or bring no performance improvements (Li et al., 2022). Before being fed into a point-based network, a down-sampling operation is often adopted to reduce the number of points to an acceptable level.

Overall, the recent efforts still remain infeasible facing our scenario: how to segment MLS oilseed rape with tiny siliques while maintaining the complete spatial information? The main challenges lie in two aspects (i) it's difficult to preserve complete spatial information of the data when the resolution of the point clouds is reduced. The widely used hard voxelization in voxel-based methods and the down-sampling operation in point-based methods both result in great information loss to the original data. Especially for oilseed rape, where dense point clouds are

pivotal for depicting its structure (Fig. 1). (ii) Training and inferring on dense voxel grids or point clouds are inefficient. Such dense data representations can bring an intolerable computational cost to the existing deep learning methods

To tackle the limitations mentioned above, we proposed a plant segmentation transformer (PST) to segment MLS oilseed rape point clouds in dense resolution. Specifically, we build up a dynamic voxel feature encoder (DVFE) to preserve and aggregate complete information of the dense inputs. Further, to achieve a better trade-off between the segmentation performance and inference time, we adopt the attention mechanism regarding its efficiency on point cloud learning and ability to capture large contextual information of the data. The experiment results have verified that PST realizes the segmentation of MLS oilseed rape with optimal performance while maintaining an acceptable inference speed. In summary, our main contributions are as follows.

(i) We propose a fully annotated MLS oilseed rape dataset containing 55 podding stage oilseed rape. The proposed dataset has been manually supervised.

(ii) We proposed an end-to-end novel network plant segmentation transformer (PST) for dense MLS oilseed rape point cloud semantic segmentation, which can segment tiny siliques in high-precise and low inference time.

(iii) We integrated the proposed network with an optimized instance segmentation head and developed PST-PG to realize instance segmentation of MLS oilseed rape point cloud.

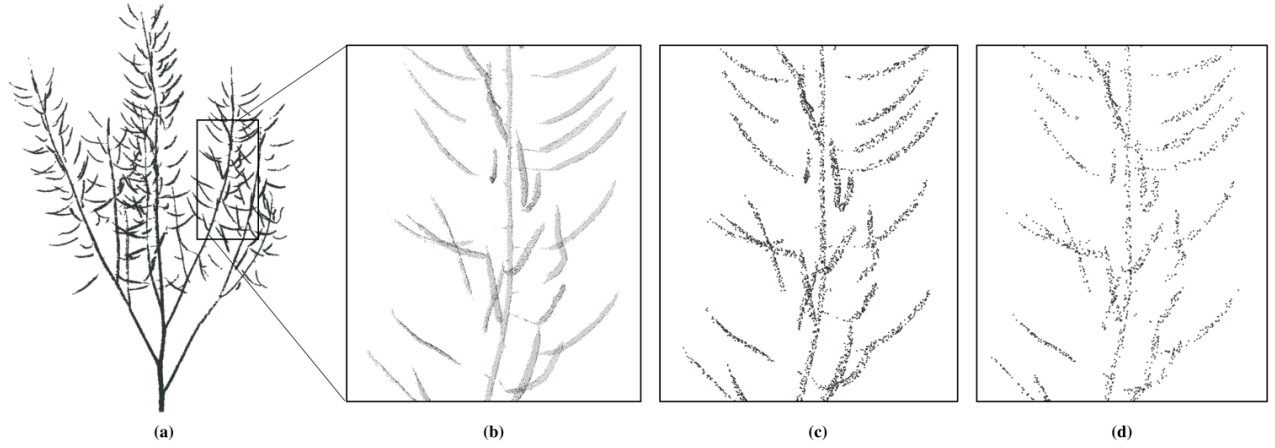


**Fig. 1.** A visualization of adopting a down-sample strategy on an MLS oilseed rape point cloud.

We crop a full-scale input(a) into a sub-patch(b) and adopt random point sampling (RPS) on it. (c) denotes the sub-patch is sampled to 8192 points, and (d) denotes the sub-patch is sampled to 4096 points. RPS is used as the mainstream down-sampling strategy. 4096 and 8192 are the numbers of points suggested for input in most existing point-based deep learning networks.

## 2. Methods

### 3.1 MLS Oilseed Rape Datasets

In this study, the oilseed rape point clouds were acquired through a mobile laser scanner (SCAN Tech. PRINCE775 laser scanner) with a maximum measurement error of 0.03mm. All the point clouds are fully annotated with manual supervision. Each point is annotated to silique or non-silique class in this study.

Though the total number of the proposed point clouds is limited, each integrated oilseed rape is large in scale and consists of plenty of morphology structure information. Since the laser



scanning directly obtains the integrated plant point cloud, the proposed point clouds are highly precise and dense, leaving out the bias and information loss during the reconstruction process in other approaches. The details of our dataset are given in Table 1.

**Table 1**

MLS oilseed rape dataset

number of plant	number of points	plant coverage ( $[length, width, height] \cdot cm$ )	average silique proportion(%)	average non- silique proportion(%)
55	$2.4 \times 10^4 - 9.52 \times 10^5$	min: [11.08, 10.69, 53.48] max: [61.47, 69.97, 132.22]	79.97	20.03

### 3.2 Data Preprocessing

In the training phase, we use a fixed-size cubic to crop integrated point clouds into patches, each treated independently in the network. And in the validation and testing phases, we partition each integrated input point cloud into patches and use a region-slide inference strategy to ensure that every point is predicted by the network.

To enrich the training data, we partition the point cloud with two offset values (0 and 8cm), resulting in two sets of different patches. Therefore, the actual annotated data for training, validating, and testing extracted from the integrated plant are enriched at a high level, assuring a large amount of data for the deep learning algorithm. The choice of patch size depends on the

properties of the input data. To ensure each patch encompasses moderate semantic information, we set the length of the patch to 16cm during the study.

### 3.3 Network Overview

As we discussed in Sec. 1, in order to segment dense point clouds without adopting a point down-sampling strategy, we consider two problems. The first is that the network can take in a dense and dynamic input of point cloud, and the second is that the network is acceptable both in computation cost and obtained segmentation results. Thus, we use a voxel-based encoder, available to any input point number, for per point feature encoding. As for the trade-off between efficiency and segmentation results, we adopt the self-attention mechanism base on the prior work (Fan et al., 2021; Liu et al., 2021). Hence, we design our plant segmentation transformer (PST) to process dense MLS oilseed rape point clouds. Fig. 2 overviews the network architecture of the PST, which follows an encoder-decoder pipeline and has three main components, *i.e.*, the dynamic voxel feature encoder (DVEF) (Fig. 2(b)), dual-window wise attention, and dense feature recover decoder.

The input to the PST is a point set  $\mathbb{P}$  with  $N$  points. Each point set has 3D coordinates  $\mathbf{P} = \{p_i\} \in \mathbb{R}^{N \times 3}$ , where  $p_i = (x_i, y_i, z_i)$  and an feature map  $\mathbf{F} = \{f_i\} \in \mathbb{R}^{N \times C_0}$ , where  $C_0$  is the channel number of the input. The input is first fed into DVEF and embedded to the voxel set  $\mathbb{V}$  with  $N_V$  voxels. We denotes  $\mathbf{V} = \{v_j\} \in \mathbb{Z}^{N_V \times 3}$  where  $v_j = (x_j^V, y_j^V, z_j^V)$  and  $\mathbf{F}^V = \{f_j^V\} \in \mathbb{R}^{N_V \times C_1}$  as the voxel-wise coordinates and the high dimension feature map of voxel  $v_j$ , respectively.

After DVEF, the voxel set is partitioned into two sets of windows with a region shift mechanism (Fan et al., 2021). Each set contains multiple non-overlapping windows. We then apply multi-head self-attention to the voxel feature map  $\mathbf{F}^V = \{f_j^V\}$  and obtain the well encoded voxel-wise output  $\mathbf{G}^V = \{g_j^V\} \in \mathbb{R}^{N_V \times C_2}$ .

Lastly,  $\mathbf{G}^V = \{g_j^V\}$  is propagated into point-wise resolution and interacted with  $\mathbf{F}$  to form the final encoded point feature set  $\mathbf{G} = \{g_i\} \in \mathbb{R}^{N \times (C_2 + C_0)}$ . We then calculate the probability scores per point based on  $\mathbf{G}$  to get the final semantic label  $\mathbf{S} = \{s_i\}$  for each point. Furthermore, we integrate our PST with an instance segmentation head to form PST-PG (Sec. 3.7) and realize precise silique instance segmentation of oilseed rape.

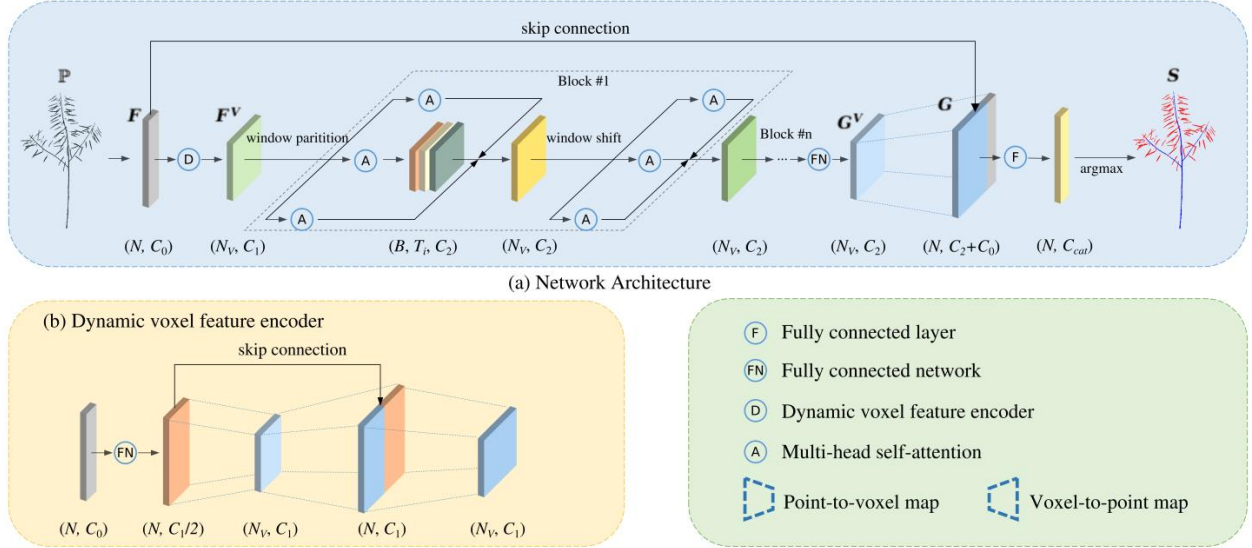


**Fig. 2.** Illustration of the PST architecture. (a) is the main component of PST, which follows an encoder-decoder pipeline. (b) is a demonstration of dynamic voxelization used in the encoding part.

### 3.4 Dynamic voxel feature encoder

Paradigm voxel-based methods usually voxelize the point clouds into dense grids and generate a one-to-many bi-directional map between every pair of  $p_i$  and  $v_j$ . A voxel has a fixed capacity  $Y$  of assigned points, so if more than  $Y$  points are assigned to a voxel, they are sub-sampled to  $Y$ . Similarly, those less than  $Y$  are zero-padded (Huang and You, 2016; Zhou and Tuzel, 2018). Such voxel representation, called hard voxelization (HV) (Zhou et al., 2019), naturally preserves the neighborhood context of 3D point clouds, leading to easy application of advanced techniques borrowed from 2D counterparts, ensuring a steady segmentation performance. However, its limitations are also intrinsic, i.e., (1) The stochastic dropout of points may cause information loss in voxelization, worsening discrimination of segmentation outcomes, especially for oilseed rape point clouds with small scale traits. (2) Zero-padded voxels also occupy computation resources.

To overcome the above issues, this study builds the dynamic voxel feature encoder (DVFE) based on dynamic voxelization (DV) (Zhou et al., 2019) for voxel feature embedding. Define  $\mathbf{M}_V(p_i)$  and  $\mathbf{M}_P(v_j)$  as the mapping functions assign each point  $p_i$  to a voxel  $v_j$  and gather the points within a voxel  $v_j$  due to their 3D coordinates, respectively. The difference between HV and DV is defined as follows (Zhou et al., 2019):

$$HV \begin{cases} M_V(p_i) = \begin{cases} \phi & p_i \text{ is dropped out} \\ v_j & i \text{ preserved after sub sampling} \end{cases} \\ M_P(v_j) = \{p_i | \forall p_i \in v_j\} \end{cases} \quad (1)$$

$$DV \begin{cases} M_V(p_i) = v_j, \forall i \\ M_P(v_j) = \{p_i | \forall p_i \in v_j\} \end{cases} \quad (2)$$

Instead of sub-sampling points to the fixed capacity  $Y$  of a voxel, DV provides a complete map between  $p_i$  and  $v_j$  without information loss. Each point is assigned to a certain voxel in terms of their spatial distance, and consequently, the number of points in the voxel is dynamic.

DVFE encodes the raw point-wise input to a voxel-wise embedding with a learned high feature. Given an input point set  $\mathbb{P}$ , the 3D space is divided into voxel grids, and each point is assigned to the voxel it occupies. We denote  $\mathbf{PC} = \{pc_i\} \in \mathbb{R}^{N \times 3}$ , where  $pc_i = (x_i^c, y_i^c, z_i^c)$  is the XYZ coordinates of the centroid of the points in the voxel  $v_j$  that point  $p_i$  belongs to, *i.e.*,

$$pc_i = \frac{1}{N^{v_j}} \sum_{k \in v_j} p_k \quad (3)$$

where  $N^{v_j}$  is the number of points in voxel  $v_j$ , and the mapping function in Eq. (3) is  $M_p(v_j) = \{p_k\}$ . With  $\mathbf{PC}$  and  $\mathbf{V}$  (Sec. 3.3), the raw input feature  $\mathbf{F}$  is now augmented as  $\hat{\mathbf{F}} = \{\hat{f}_i\}$ , where  $\hat{f}_i = (x_i, y_i, z_i, x_i - x_i^c, y_i - y_i^c, z_i - z_i^c, x_i - x_j^v, y_i - y_j^v, z_i - z_j^v) \in \mathbb{R}^9$ . Next, two consecutive VFE layers (Sindagi et al., 2019; Zhou and Tuzel, 2018), each consisting of a fully connected network, are applied to obtain a voxel-wise high dimension feature map  $\mathbf{F}^V = \{f_j^V\}$ , the above operation can be defined as:

$$\hat{\mathbf{F}}^V = \Lambda_{M_V}(FCN(\hat{\mathbf{F}})) \quad (4)$$

$$\mathbf{F}^V = \Lambda_{M_V}(FCN(Concat(V_{M_p}(\hat{\mathbf{F}}^V), FCN(\hat{\mathbf{F}}))) \quad (5)$$

Eq. (4) and Eq. (5) are the first and the second VFE layer, respectively, where  $\Lambda_{M_V}$  refers to the aggregation function, *i.e.*, average, max, or sum in terms of the mapping function  $M_V$ .  $V_{M_p}$  refers to the propagation function that recovers voxel-wise feature map to point-wise feature map

in terms of  $M_p$ .  $FCN$  represents the fully connected network composed of a fully connected layer, a batch normalization layer, and an activation function. The first VFE layer aggregates the decorated point features belonging to a specific voxel using the max-pooling (i.e.,  $\Lambda_{M_V}$ ) to a voxel-wise feature map  $\hat{F}^V$ . The second VFE layer propagates  $\hat{F}^V$  using  $V_{M_p}$  and concatenates it with the learned point features. Finally,  $\Lambda_{M_V}$  is used again to aggregate the final feature embedding of DVEF. Simplified VFE layers is shown in Fig. 3(a). Note that a sequent operation of  $V_{M_p}(\Lambda_{M_V}(F))$  is not equal to  $F$  (Fig. 3(b)).

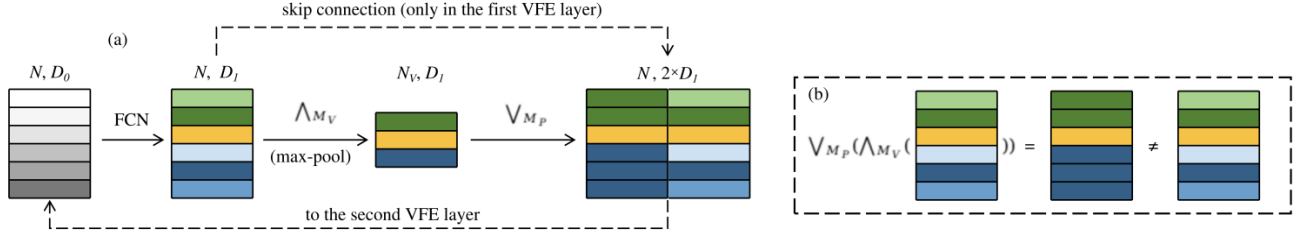


**Fig. 3.** Illustration of the simplified VFE layers in DVFE.

For simplicity and clarity, we adopt the coordinates  $\mathbf{P}$  as the initial features  $\mathbf{F}$  of the input fed into DVEF (i.e.,  $\mathbf{P}=\mathbf{F}$ ) in this study. Other features like reflectance, RGB, or normal can easily be used by changing the channel numbers.

### 3.5 Dual window sets attention

After the DVFE, the voxel features have captured a preliminary abstraction of the aggregated point features; however, it lacks the local contextual information between voxels. As discussed in Sec. 3.3, we adopt the attention mechanism to increase the receptive field and capture the local context. Directly applying the attention mechanism on a global scale of voxel embedding is

undesirable, leading to a dilemma between a precise performance and a scalable computation cost since immense representatives of voxels are required for satisfying results. Therefore, we adopt the *shifted-window* self-attention approach following the prior work in Single Stride Transformer (Fan et al., 2021), which has been proven to be very effective in the 2D image and autonomous driving scenarios.

### **Window partitioning and shifting**

PST partitions the voxel grids into non-overlapping axis-aligned windows for computing self-attention locally in each window. The number of voxels divided into the window is controlled by hyper-parameters. Supposing the size of the window is  $(l_x^W, l_y^W, l_z^W)$ . Thus each window contains  $l_x^W \times l_y^W \times l_z^W$  voxels for the calculation of their semantic affinities. Further, the origin partitioned window-wise set is shifted at a Euclidean distance of  $(\frac{l_x^W}{2}, \frac{l_y^W}{2}, \frac{l_z^W}{2})$  to form a new set for building connections across windows and enriching the contextual information. Consequently, two sets containing multiple windows, illustrated as “dual window sets”, are obtained.

### **Self-attention in dual window sets**

As the points are distributed sparsely in the 3D space, only the voxels assigned at least one point are seen as valid, while the unoccupied ones are invalid. Thus the number of valid voxels in each window varies. To handle such sparsity, PST divides the windows into sub-batches regarding the number of valid voxels within. Given the number of total voxels in a window  $N_V^W = l_x^W \times l_y^W \times l_z^W$ , the sub-batches are divided as in Table 2.:

**Table 2**

Sub-batches in training and inference phases

phase	sub-batch	number of valid voxels	voxels padding
training	1	$0 \sim 0.25N_V^W$	$0.25N_V^W$
	2	$0.25 \sim 0.5N_V^W$	$0.5N_V^W$
	3	$0.5 \sim 1N_V^W$	$0.9N_V^W$
inference	1	$0.25 \sim 0.5N_V^W$	$0.5N_V^W$
	2	$0.25 \sim 0.5N_V^W$	$0.5N_V^W$
	3	$0.5 \sim 0.9N_V^W$	$0.9N_V^W$
	4	$0.9 \sim 1N_V^W$	$N_V^W$

The windows containing a similar level of valid voxels are divided into the same sub-batch. Then the number of voxels in each window is padded to the same value (Table 2. voxel padding) so that the self-attention within each window in a sub-batch can be calculated in parallel.

Specifically, to add variance in the training phase, we set the highest padding level as  $0.9N_V^W$ , which means a window with more than  $0.9N_V^W$  valid voxels will be randomly sampled to  $0.9N_V^W$ .

Finally, the self-attention in dual window sets are computed as:

$$\text{set 1} \quad \begin{cases} \tilde{F}_i^V = MSA(LN(F_{i-1}^V), PE(V_{i-1})) + F_{i-1}^V \\ F_i^V = MLP(\tilde{F}_i^V) + \tilde{F}_i^V \end{cases} \quad (6)$$

$$\text{set 2} \quad \begin{cases} \tilde{F}_{i+1}^V = MSA(LN(F_i^V), PE(V_i)) + F_i^V \\ F_{i+1}^V = MLP(\tilde{F}_{i+1}^V) + \tilde{F}_{i+1}^V \end{cases} \quad (7)$$

where  $MSA$  is multi-head self-attention module,  $LN$  is layer normalization,  $PE$  denotes the position encoding function in (Carion et al., 2020).  $\tilde{F}_i^V$  and  $F_i^V$  are the voxel-wise output feature



map of the *MSA* and *MLP* module in block  $i$  (in this study  $i=6$ ), respectively.

### 3.6 Dense feature propagation

The final output  $\mathbf{G}^V$  is well encoded after several dual window-sets attention blocks. To obtain a dense point-wise encoded feature map  $\mathbf{G}$  for computing the semantic labels  $\mathbf{S}$  per point, we first recover  $\mathbf{G}^V$  to its point-wise resolution using the propagation function  $V_{Mp}$  as in DFEF(Sec. 3.4). Second, we concatenate the propagated feature map with a learned input  $\mathbf{F}$  to build up interaction between them and enrich the semantic granularity of  $\mathbf{G}$ . Then,  $\mathbf{G}$  with the dimension of  $N \times C_2$  is transformed to  $N \times C_{cls}$  by a fully connected layer, where  $C_{cls}$  is the number of semantic classes. In this study we set  $C_{cls}=2$  (i.e., siliques and non-siliques). Finally, the probability scores per point for all classes are computed by carrying out a softmax operation, and the class with the highest probability is assigned to that point. The above operation can be defined as:

$$\mathbf{G} = \text{Concat}(V_{Mp}(\mathbf{G}^V), \text{MLP}(\mathbf{F})) \quad (8)$$

$$\mathbf{S} = \text{Argmax}(\text{Softmax}(\text{FC}(\mathbf{G}))) \quad (9)$$

In the training phase, the network takes random patches from the training dataset at an amount of batch size in each iteration. Consequently, the training patches may not cover all the points in an input point cloud. Such training approaches ensure the robustness of the network. However, in the inference phase, to obtain complete segmentation labels of the input point cloud without losing a point, we adopt a region-slide strategy with an overlap to traverse every point. The final semantic

label assigned to each point is obtained on the averaged probability scores.

### **3.7 Integration with instance segmentation**

A two-stage pipeline considering instance segmentation as a subsequent clustering stage after semantic segmentation is widely used in the design of an end-to-end instance segmentation network (Elich et al., 2019; Han et al., 2020; Mo et al., 2019; Pham et al., 2019; Wang et al., 2018). In such a pipeline, the points with semantic labels predicted in the first stage are grouped into instances by an instance segmentation head in the second stage. Inspired by Jiang et al. (2020), we combine PST with the instance segmentation head in PointGroup (PG) and form PST-PT (Fig. 4) to achieve the instance segmentation of siliques in oilseed rapes. The contextual and morphology traits are well abstracted by PST, which provides discriminative point-wise features for the subsequent processing in the second stage.

We choose the instance segmentation head in PG as the base network of our second stage mainly for two reasons: (i) PG is developed in a hybrid-model manner, making it flexible when hybridizing with other models (i.e., PST) served in the first or second stage. (ii) PG leverages the void space between instances to increase the performance of instance segmentation. Since the void space between each silique in a naturally ripened oilseed rape is also quite regular, it can be an effective backup in our scenario.

### 3.7.1 Instance segmentation head in PointGroup

This section briefly revisits the instance segmentation head in PG for completeness. The network mainly contains three parts: (i) learn a per-point offset vector to shift each point to its corresponding instance centroid; (ii) use a clustering algorithm to group points with semantic predictions into candidate clusters in the original coordinate space and shifted coordinate space; (iii) predict the scores for each candidate using ScoreNet to select the proper cluster.

Given a point  $i$ , the void space-based clustering algorithm neighbors the points within an  $r$ -sphere centered at  $p_i = (x_i, y_i, z_i)$ , where  $r$  serves as a spatial threshold, and groups points with the same semantic labels as  $i$  into the same candidate cluster. Here, points with distances larger than  $r$  or in different classes will not be grouped. However, clustering only in the original coordinate space may wrongly group the same-class instances close to each other. Thus, a sub-branch network is trained to learn an offset  $\mathbf{OS} = \{os_i\} \in \mathbb{R}^{N \times 3}$  for shifting each point in  $\mathbf{P} = \{p_i\}$  towards its instance centroid. In the shifted coordinate set  $\mathbf{P}^S = \mathbf{P} + \mathbf{OS} \in \mathbb{R}^{N \times 3}$ , the void space between the instances increases so that the adjacent same-class instances can be discriminated better.

Denote  $\mathcal{C}^O$  and  $\mathcal{C}^S$  as the clustering results on the original coordinate set  $\mathbf{P}$  and the shifted coordinate set  $\mathbf{P}^S$ , respectively. PointGroup then constructs a ScoreNet to predict a score for each candidate cluster in  $\mathcal{C} = \mathcal{C}^O \cup \mathcal{C}^S$  to describe their quality. In the inference phase, the non-maximum suppression(NMS) is adopted on the clusters to quantify their quality so that the acceptable ones can be added to the final instance predictions.

As for the loss functions, we use a standard cross-entropy loss  $L_{c\_sem}$  for the semantic branch(i.e., PST) in the first stage. In the second stage, we adopt the same settings as in PG. Specifically, for the offset prediction branch, two loss functions are adopted. One is a  $L_1$  regression loss  $L_{o\_reg}$  to constrain the  $L_1$  norm between each point and its corresponding instance centroid. The other is a direction loss  $L_{o\_dir}$  (Lahoud et al., 2019) to ensure each point moves towards its centroid. For ScoreNet, the loss function is a binary cross-entropy loss as  $L_{c\_score}$ .

### 3.7.2 Variants of PST-PG

#### V-PST-PG

We build the base version of PST-PG, called Vanilla(V)-PST-PG, as in Fig. 4. In the implementation of V-PST-PG, we feed  $\mathbf{F}$  in two branches, one for semantic segmentation(i.e., PST) to obtain class labels  $\mathbf{S}$ , the other for predicting the offset  $\mathbf{OS}$  to shift the original coordinates  $\mathbf{P}$  to  $\mathbf{P}^S$ . As we are only concerned with the silique instances, the non-silique predictions from PST are masked and have no effect during the clustering part.

After clustering, supposing the total number of candidate clusters is  $M$  and  $N_i^C$  denotes the number of points in  $C_i$ , that is  $\mathbf{C} = \{C_i\} \in \mathbb{R}^{M \times N_i^C \times 3}$ . we then gather the high-dimensional point feature  $\mathbf{G} = \{g_i\}$  followed by an extra *MLP* layer from PST for each cluster and form a cluster-wise feature set  $\mathbf{F}^C = \{f_i^C\} \in \mathbb{R}^{M \times N_i^C \times C_3}$  as the input to ScoreNet. The final cluster scores  $\mathbf{S}^C = \{s_i^C\} \in \mathbb{R}^W$  are obtained as :

$$S^C = \text{Sigmoid}(\text{MLP}(\text{ScoreNet}(F^C, C))) \quad (10)$$

V-PST-PG is trained in an end-to end manner following the initial configuration as in PG. The clustering and ScoreNet are not activated in training until the semantic and the offset prediction branches arrive at the preparation epoch. After the preparation epoch, all components in V-PST-PG are trained simultaneously. The total loss function for V-PST-PG is defined as:

$$L_{v\_ins} = \begin{cases} L_{c\_sem} + L_{o\_reg} + L_{o\_dir} & \text{epoch} \leq \text{preparation epoch} \\ L_{c\_sem} + L_{o\_reg} + L_{o\_dir} + L_{c\_score} & \text{epoch} > \text{preparation epoch} \end{cases} \quad (11)$$

### F-PST-PG

Inspired by (Brock et al., 2017), as long as the semantic branch is capable of providing ideal and stable semantic predictions for the subsequent training. It is unnecessary to have PST participate after the preparation epoch. Thus, we freeze the PST by excluding them from the backward pass after the preparation epoch to form F-PST-PG (i.e., PG with frozen PST). Unlike V-PST-PG, where the semantic output  $\mathbf{S}$  changes after every training iteration, in the implementation of F-PST-PG, once PST is well trained, the semantic output  $\mathbf{S}$  is fixed and serves as the fixed-learned supervision for the instance segmentation head. The total loss function for F-PST-PG is defined as:

$$L_{f\_ins} = \begin{cases} L_{c\_sem} + L_{o\_reg} + L_{o\_dir} & \text{epoch} \leq \text{preparation epoch} \\ L_{o\_reg} + L_{o\_dir} + L_{c\_score} & \text{epoch} > \text{preparation epoch} \end{cases} \quad (12)$$

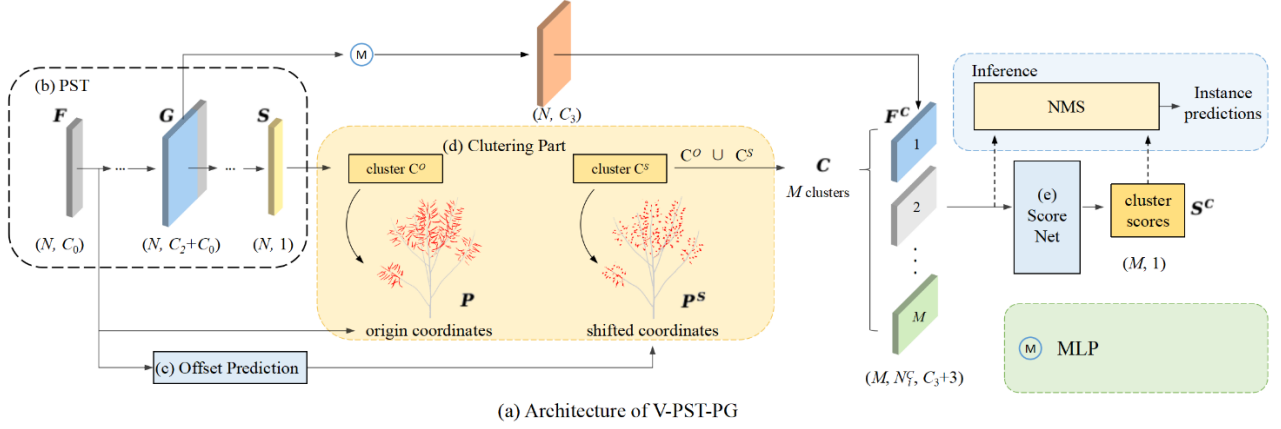


**Fig. 4.** Illustration of VPST-PT, which consists of four parts: PST(b), offset prediction(c), the clustering part (d), and ScoreNet (e).

### 3.8 Network training and testing

#### Implementation details

All the experiments in this study are conducted on the Pytorch platform. Specifically, we design the proposed network PST/PST-PG and compare different baseline models (Sec. 4.6) based on the open repository of OpenMMLab.

As for the setup details of PST, in dynamic voxel feature encoder(DVFE), the voxel size used in dynamic voxelization (DV) is  $0.6\text{cm} \times 0.6\text{cm} \times 0.25\text{cm}$ , and the aggregate function is max-pooling. In dual window sets attention, the window size is  $6 \times 6 \times 12$ , which means the total number of voxels within the window(i.e.  $N_V^W$ ) is 432. In dense feature propagation, the overlap for region-slide inference is 8cm (half of the patch size). Thus a validation or testing patch is predicted twice to obtain the final average probability scores.

We build up the instance segmentation head and implement the second stage of PST-PG

adopting the same settings in PointGroup. Please refer to (Jiang et al., 2020) for details.

## **Training**

We train PST using AdamW optimizer with a weight decay of 0.05 and the cyclic learning rate schedule. The base learning rate is  $10^{-5}$ , and the maximum learning rate is  $10^{-3}$ . During the training, the batch size is set to 4. The network is evaluated every two epochs on the validation set and trained until the loss is stable both on the training and validation sets.

## **Testing**

For testing, the batch size is set to 1, and the learned parameters of PST for testing are determined in terms of the lowest loss on the validation set.

## **3.9 Evaluation metrics**

In this study, we evaluate the semantic segmentation network (i.e., PST) and the instance segmentation network (i.e., PST-PG) separately.

For semantic segmentation, we evaluate Intersection-over-Union(IoU), Precision(Prec), Recall(Rec), and F1-score four class-level metrics and one global metric, overall accuracy(oAcc). Specifically, for each semantic class, IoU is known for measuring overlap between predicted points and ground truth points. Prec and Rec measure the correctly predicted points to the total predicted points and total ground truth points, respectively. F1-score is defined as the harmonic mean of Prec and Rec. Across all the classes, oAcc is the proportion of total correctly predicted points to the total number of points. We also include these results for comparison (Sec. 4.6). The five metrics are

defined as:

$$IOU = \frac{TP_C}{TP_C + FP_C + FN_C} \quad (13)$$

$$Prec = \frac{TP_C}{TP_C + FP_C} \quad (14)$$

$$Rec = \frac{TP_C}{TP_C + FN_C} \quad (15)$$

$$F1 = 2 \frac{Prec \cdot Rec}{Prec + Rec} \quad (16)$$

$$oAcc = \frac{TP + TN}{TP + TN + FP + FN} \quad (17)$$

where  $TP_C$ ,  $FP_C$ ,  $FN_C$  are the number of true positive, false positive, and false negative points for a certain class  $Cls$ , respectively. In this study,  $Cls \in \{\text{silique}, \text{non} - \text{silique}\}$ .

For instance segmentation, we use mean precision(mPrec), mean recall(mRec), mean coverage(mCov) and mean weighted coverage(mWCov) (Li et al., 2022; Liu et al., 2017; Ren and Zemel, 2017; Wang et al., 2019a; Zhuo et al., 2017). Specifically,  $mPrec_\theta$ , and  $mRec_\theta$  denote the mPrec and mRec with the IoU threshold set to  $\theta$ . mCov is the average IoU of instance prediction matched with ground truth. mWCov is calculated as mCov weighted by the size of each ground truth instance. The four metrics are defined as:

$$mPrec_\theta = \frac{TP_\theta^{ins}}{|O|} \quad (18)$$

$$mRec_\theta = \frac{TP_\theta^{ins}}{|R|} \quad (19)$$



$$mCov = \frac{1}{|R|} \sum_{i=1}^{|R|} \max_j IoU(P_i^R, P_j^O) \quad (20)$$

$$mWCov = \sum_{i=1}^{|R|} w_i \max_j IoU(P_i^R, P_j^O) \quad (21)$$

$$w_i = \frac{|P_i^R|}{\sum_k |P_k^R|} \quad (22)$$

where  $TP_{\theta}^{ins}$  is the number of predicted instance having an IoU larger than  $\theta$  with the ground truth.  $|R|$  and  $|O|$  is the number of all instances in the ground truth and prediction, respectively. In Eq. 19 and Eq.20,  $|P_i^R|$  is the number of points in the  $i$ -th ground truth instance, and  $|P_j^O|$  is the number of points in the  $j$ -th predicted instance.

## 4. Results

### Dataset split

The MLS oilseed rape datasets are split into training, validation, and testing sets. Specifically, sample 1-40 are used for training, sample 41-49 are used for validation, and sample 50-55 are used for testing.

In the ablation study and hyper-parameters choosing, we train on the training set and report results on the validation set. In the evaluation and comparison with other approaches, we train on the training set and report the results on the testing set. We also implement six-fold cross-validation

on sample 1-55.

#### 4.1 Semantic segmentation

We report the performance of the proposed semantic segmentation network PST and compare it with several popular counterparts on the testing set. To achieve a fair comparison, we conduct all the experiments on the open framework MMDetection3D in this section. For the network setting and parameters selection, we follow the configuration from their original papers. The results are listed in Table 3.

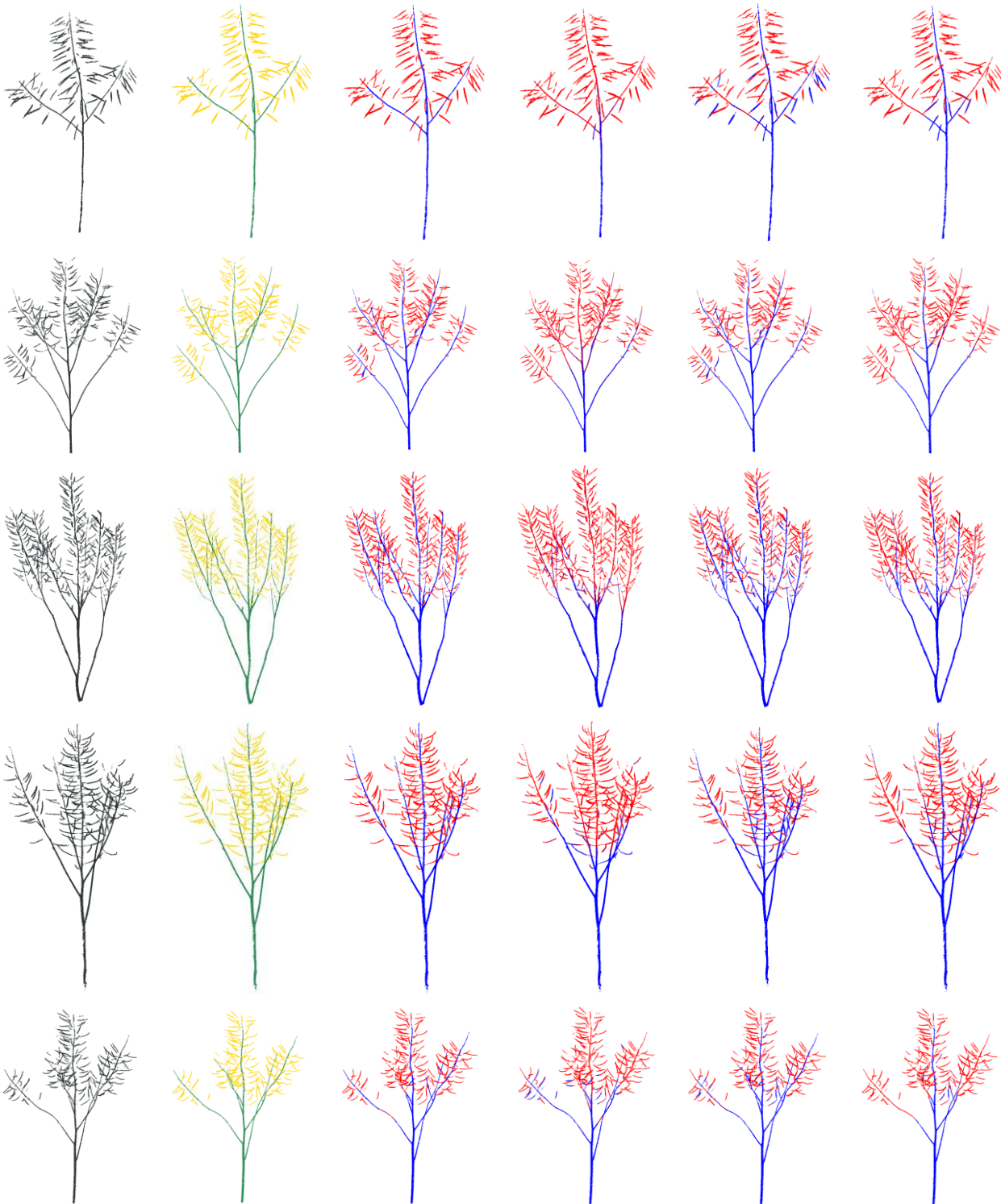
PST outperforms all the counterpart networks with the highest performance in IoU (93.96%), precision (97.29), recall (96.52), F1-score (96.88), and overall accuracy (97.07%). The improvement of these metrics compared to the second-best results achieved by PAConv are 7.62%, 3.28%, 4.8%, 4.25%, and 3.88%. The display in Fig. 5 is of testing samples with diverse tiller-number to estimate the segmentation ability of four networks. Though siliques are of small scale and scattered closely among the oilseed rape branches (i.e., non-silique) in the 3D space, making them hard to be extracted, PST still has the best sensitivity and accuracy in distinguishing them. PointNet++ (MSG) (Qi et al., 2017b) serves as the most effective network among the PointNet family, often failing to recognize the branches in the canopy and consider all the objects as an ensemble in that region, achieving the worst results across all the networks. PAConv (Xu et al., 2021) is built up based on PointNet using an adaptive convolution mechanism to learn contextual information. It has a better discernibility in the canopy than the other two counterparts. However,

we notice that in the junction region where the stem tillers, the performance of PAConv deteriorates as the structure becomes complex. The graph-based method DGCNN considers point clouds as spatial graphs and focuses on the edge information of the constructed graphs. The performance of DGCNN (Wang et al., 2019b) is placed between PointNet++ and PAConv as it may ignore the branches and often confuse the intra-class points.

**Table 3**

The comparison of semantic segmentation across the four networks. The best results are in boldface.

Method		IoU(%)	Prec(%)	Rec(%)	F1(%)	oAcc(%)
PointNet++	silique	85.33	89.20	95.16	92.08	
	non-silique	75.71	91.34	81.56	86.18	
	mean	80.52	90.27	88.36	89.13	89.93
PAConv	silique	89.86	91.46	98.09	94.66	
	non-silique	82.82	96.55	85.35	90.60	
	mean	86.34	94.01	91.72	92.63	93.19
DGCNN	silique	86.71	89.77	96.22	92.88	
	non-silique	77.76	93.17	82.46	87.49	
	mean	82.24	91.47	89.34	90.19	90.93
PST (Ours)	silique	95.40	96.43	98.89	97.65	
	non-silique	92.51	98.15	94.15	96.11	
	mean	<b>93.96</b>	<b>97.29</b>	<b>96.52</b>	<b>96.88</b>	<b>97.07</b>



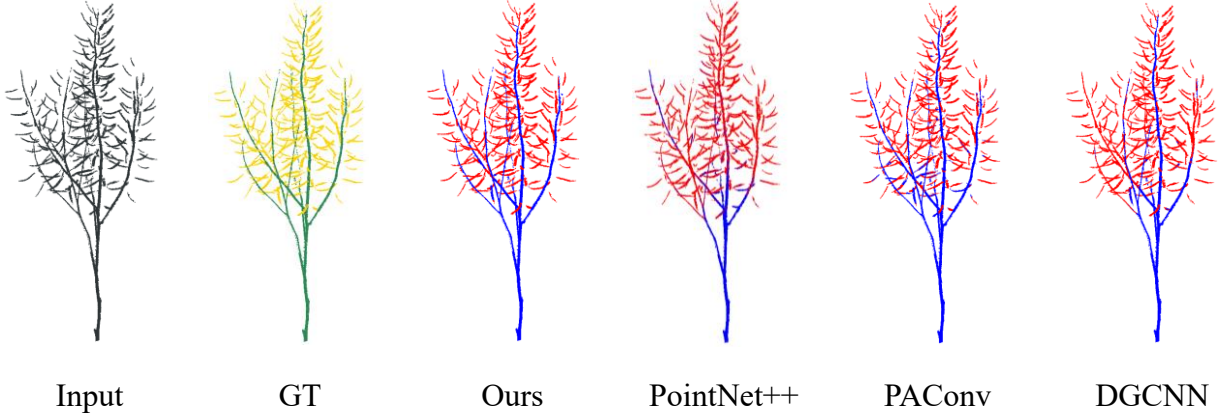


**Fig. 5.** Illustration of the qualitative results on the testing set.

### **Six-fold cross validation**

We evaluate PST by six-fold cross-validation on the whole dataset (Fig. 6). Each sample is treated as the testing data once. PST performs more stable on segmenting siliques than non-siliques slightly with a lower standard deviation(STEDV) of IoU(1.46) and F1-score(0.79). In summary, PST achieves satisfying stability on MLS oilseed rape data with 1.23 and 0.68 on STEDV of mIoU and overall accuracy(oAcc), respectively.

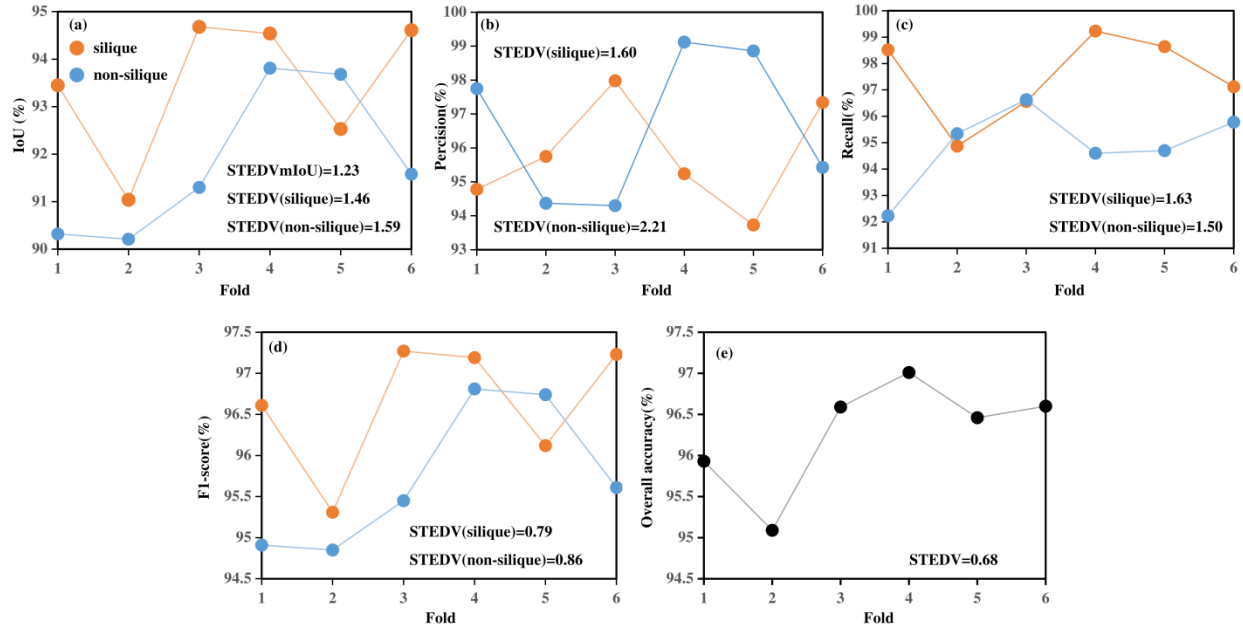


**Fig. 6.** Results of IoU(a), precision(b), recall(c), F1-score(d) and overall accuracy(e) under a six-fold cross validation.

## 4.2 Inference time analysis

For the potential of being applied in phenotyping, we are concerned with the inference time of a deep learning network. We test each method several times on an NVIDIA GeForce RTX 3090 GPU to get the average inference time listed in Table 4. PST takes the full scale of point clouds as inputs without adopting down-sampling strategies, while the other counterparts only accept fix size inputs for inference, which may consume computation resources on extra traversing in order to obtain the same resolution outputs as PST. PST ranks front among different testing groups with 156.2ms to predict a full-scale point cloud, reflecting a high potential for being used in real-time phenotyping tasks.

**Table 4**

The inference time per point cloud of the four networks. We sample the points in a patch to a certain number (i.e., Input points) to satisfy the input requirement of that network. Full-scale means we use the original point clouds without sampling as inputs.

Method	Input points	mIoU (%)	Inference time per point cloud (ms)
PointNet++	8k	64.84	58.5
PointNet++	38.4k	80.52	91.9
PAConv	8k	85.59	195.7
PAConv	20.4k	86.34	139.3
DGCNN	8k	80.37	258.4
DGCNN	20.4k	82.24	336.7
DGCNN	38.4k	77.71	497.5
PST(Ours)	full-scale	93.96	156.2

### 4.3 Instance segmentation

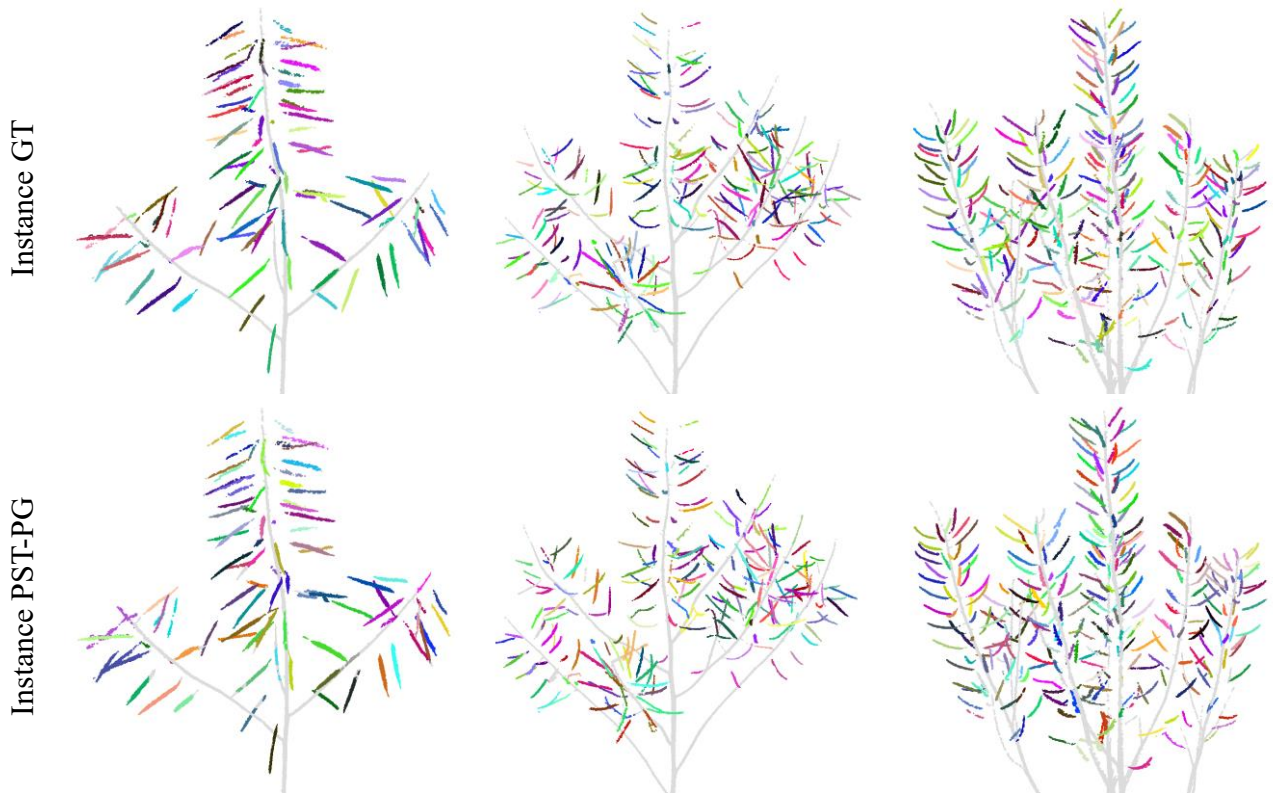
To evaluate the performance of PST as being integrated with the current instance segmentation head, we compare the instance segmentation results of the original PointGroup(PG), vanilla PST-PG, and frozen PST-PG listed in Table 5. The performance of two revised PST-PG networks has both improved compared to the original PG in mCov, mWCov, and mPrec, mRec with higher IoU threshold, demonstrating the effectiveness of PST for passing discriminative point features to the subsequent network. Specifically, F-PST-PG reaches the highest performance in the strictest mPrec and mRec with an IoU threshold of 90%, getting 88.83% on mPrec<sub>90</sub> and 82.53% on mRec<sub>90</sub>. The

visual illustrations of F-PST-PG over the testing set are shown in Fig. 7.

**Table 5**

The comparison of instance segmentation of the original PG, V-PST-PG, and F-PST-PG. The best results are in boldface.

Method	mCov	mWCov	mPrec <sub>50</sub>	mRec <sub>50</sub>	mPrec <sub>75</sub>	mRec <sub>75</sub>	mPrec <sub>90</sub>	mRec <sub>90</sub>
PG	86.58	87.64	<b>97.41</b>	84.43	90.72	78.63	86.84	76.63
V-PST-PG	89.29	89.66	97.10	89.79	<b>91.30</b>	84.42	88.21	81.57
F-PST-PG	<b>89.51</b>	<b>89.85</b>	96.66	<b>90.05</b>	91.27	<b>85.03</b>	<b>88.83</b>	<b>82.53</b>





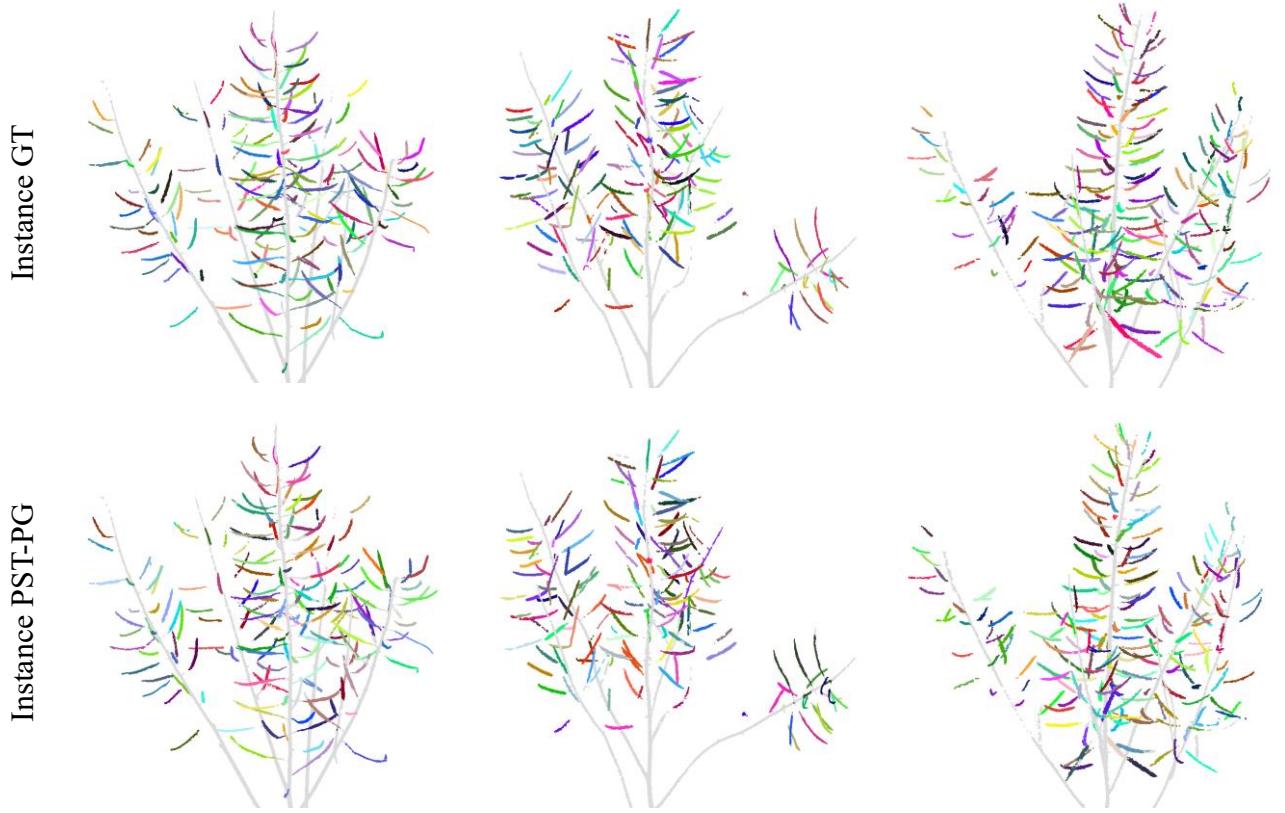


**Fig. 7.** Illustration of the qualitative results on the testing set of F-PST-PG. As we are only concerned with silique instances of oilseed rape, each silique instance is labeled with a random color, and the non-silique parts are ignored and set as gray.

We further count the number of silique instances detected by the original PG and F-PST-PG with the ground truth under the first two strict standards (Fig. 8). A predicted silique instance is counted when it has an IoU larger than 75%(Fig. 8(a)) or 90%(Fig. 8(b)) with the ground truth instance collections. For both situations, F-PST-PG performs better than the original PG. The RMSE of F-PST-PG is 20.09 when  $\text{IoU} > 75\%$  and 25.87 when  $\text{IoU} > 90\%$  on the testing samples with the average silique instance number 109, which means the undetected silique instance should be less than 20.09(when  $\text{IoU} > 75\%$ ) or 25.87(when  $\text{IoU} > 90\%$ ) when the number of silique instances

of oilseed rape is 109. We also notice that when detecting samples with more than 200 siliques, F-PST-PG outperforms PG by a big margin, indicating the effectiveness of F-PST-PG when facing complex samples.

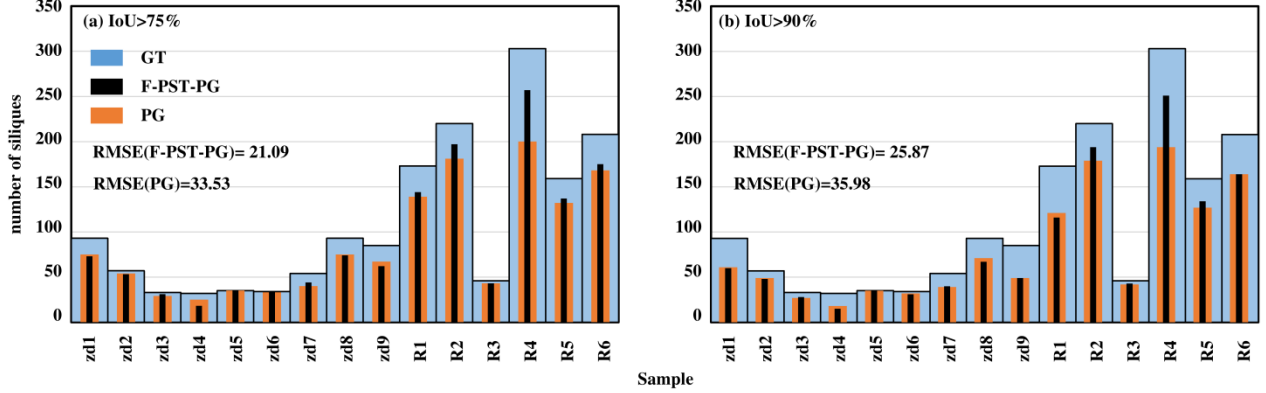


**Fig. 8.** The number of silique instances detected by F-PST-PG on the testing samples compared with the original PG and ground truth. The blue bar(widest) is the ground truth instance number for each sample. The orange bar is the instance number detected by the original PG. The black bar(narrowest) is the instance number detected by F-PST-PG.

## 5 Discussion

### 5.1 Ablation study on stacked point features in DVFE

As we discussed in Sec. 3.4, the raw point feature set is augmented by stacking each point feature with extra information before being fed into DVFE. Here, we conduct an ablation study on the validation set to analyze the choice of augmented features in DVFE. The features provided by cluster centroid per point are chosen as primitives. Besides, we consider using the corresponding

voxel centroid (i.e., voxel coordinate) and L2 norm of each point for feature augmentation.

Table 6 reports the performance of PST under different settings. This indicates that using the combination of cluster and voxel centroid ensures the best performance of PST, where mIoU on the validation set deteriorates when adding L2 norm per point. Indeed, L2 norms are calculated based on the point coordinates on a global scale, while the adoption of two centroids tends to capture the contextual information within a local region (i.e., a cluster of points and a voxel). Consequently, the local feature values provided by these two centroids are relatively small compared to L2 norms, resulting in an insufficient output with imbalance feature weights.

**Table 6**

Ablation results for PST with different augmented features on the validation set.  $x^C, y^C, z^C$  refers to the cluster centroid.  $x^V, y^V, z^V$  refers to the voxel centroid.  $\|p\|_2$  refers to L2 norm.

$x^C, y^C, z^C$	$x^V, y^V, z^V$	$\ p\ _2$	mIoU
✓			94.00
✓		✓	93.85
✓	✓		<b>94.65</b>
✓	✓	✓	93.06

## 5.2 The voxel size in dynamic voxelization

The variations in voxel size used in dynamic voxelization can cause different semantic distributions between the original point cloud and its counterpart after voxelization. In this study, each voxel is represented as  $l \times w \times h$  (*length*  $\times$  *width*  $\times$  *height*). We compare the semantic

proportion of silique and non-silique after voxelization under four different situations:  $l=w>h$ ,  $l=w>h$ ,  $l<w=h$  and  $l=w=h$ . Specifically, all the point clouds are normalized in a  $1\text{m}^3$  cubic during the experiment. Therefore, we use the voxel with  $0.6\text{cm}$ ,  $0.6\text{cm}$ ,  $0.25\text{ cm}$  for  $l=w>h$ ,  $l=w>h$ ,  $l<w=h$  and the voxel with  $0.45\text{cm}\times 0.45\text{cm}\times 0.45\text{ cm}$  for  $l=w=h$  since they output a similar number of voxels in a  $1\text{m}^3$  cubic, leading to a fair comparison of four situations with similar resolution.

As shown in Fig. 9, the proportion of both silique and non-silique after voxelization under the voxel with  $l=w>h$  achieved the best match with the initial proportion, which means using a flat voxel outperforms others, and even a normalized voxel when fitting the distribution of the original data. In addition, the bottle-up growth pattern of oilseed rape makes it more distinguishable in terms of a height-aligned perspective.

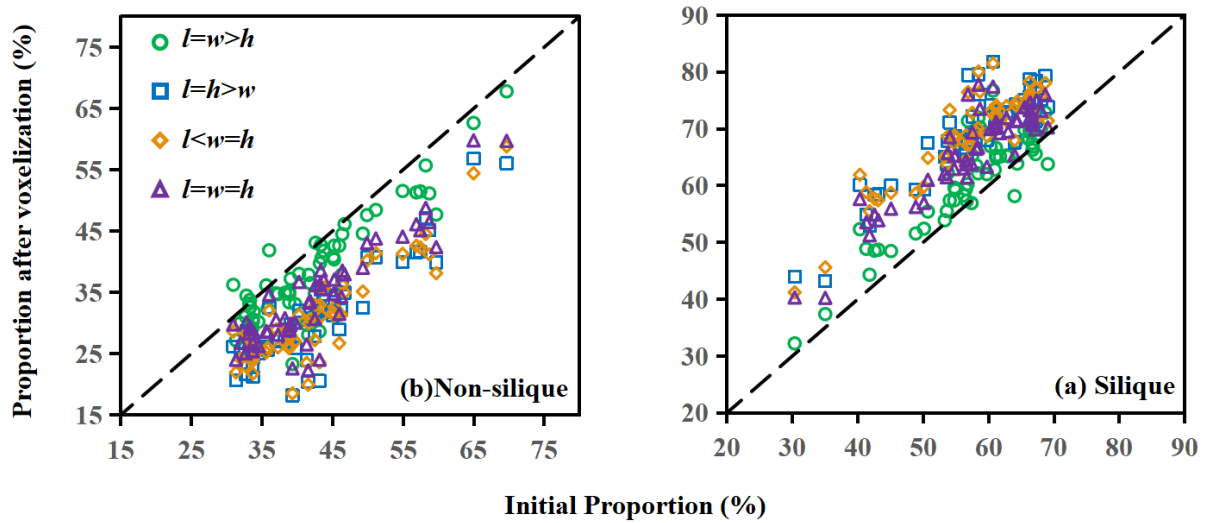


**Fig. 9.** Distribution of the silique proportion after dynamic voxelization with different voxel size.

Two different voxel sizes (*length* ( $l$ ), *width* ( $w$ ), *height* ( $h$ )) are used to form four situation:  $0.6\text{cm}$ ,  $0.6\text{cm}$ ,  $0.25\text{ cm}$  for  $l=w>h$ ,  $l=w>h$ ,  $l<w=h$  and  $0.45\text{cm}\times 0.45\text{cm}\times 0.45\text{ cm}$  for  $l=w=h$ .

### 5.3 Qualitative analysis of misclassified silique instance predictions

There are two main mistakes in the final outputs of silique instance predictions. (i) nearby different silique may be seen as one. (ii) part of the branch (i.e., non-silique) instances may be seen as siliques. We visualize the original coordinates and shifted coordinates in Fig. 10. It appears that the main reasons are from both the offset prediction branch and the semantic branch (i.e., PST). In offset prediction, the complex distribution of slim siliques makes the network hard to regress every silique to its respective centroid. Nearby siliques with boundary overlap may shift to the point between them (Fig. 10(b1)). In the semantic branch, the wrongly predicted semantic labels from PST make the network apply coordinates shift on non-silique points, resulting in mistaken candidate clusters in both the original coordinate space and shifted coordinate space.

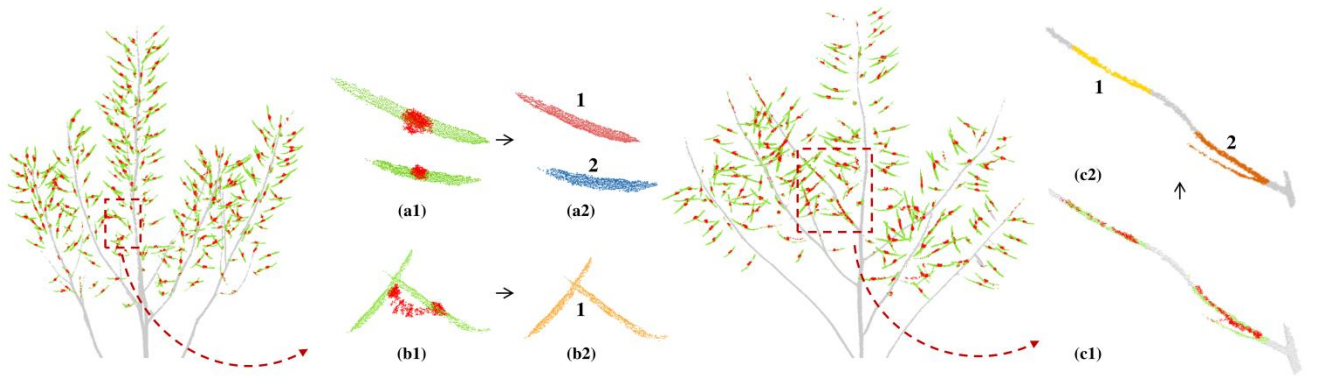


**Fig. 10.** Visualization of shifted coordinates set (red) and original coordinates set (green). (a1) is the example of well-shifted siliques, and (a2): correctly predicted siliques. (b1) shows nearby siliques shift to one centroid, and (b2): nearby siliques are predicted as one. (c1) denotes the mis-shift on the wrong semantic labels, and (c2) parts of a branch instance are predicted as siliques.

## 6. Conclusion

The common practice of using the hard voxelization or down-sampling strategy for point cloud segmentation limits the 3D phenotyping to simple plant samples, which is hard to generalize to dense plant point clouds with complex structures. To reflect this scenario for clarity, we choose the MLS oilseed rape point clouds as a typical representation, whose morphology traits are complex, and the contextual information is highly susceptible to the density of the points. To segment MLS oilseed rape point clouds, we adopt the dynamic voxelization and attention mechanism to realize per point feature learning without deteriorating the spatial information of the raw inputs. The proposed networks PST directly learn from raw inputs with dense spatial resolution and achieve an excellent trade-off between the segmentation results and inference time. Moreover, PST can feasibly integrate with other two-stage networks as the semantic segmentation head to provide discriminative semantic labels for subsequent processes. Experiment results show that PST/PST-PG outperforms the state-of-the-art counterparts in semantic and instance segmentation of MLS oilseed rape point clouds. Without elaborated optimization, PST achieved the mean IoU of 93.96%, mean Precision of 97.29%, mean Recall of 96.52%, mean F1-score of 96.88%, and overall accuracy of 97.07% with an average inference time of 156.2ms per point cloud. PST-PG achieve 89.51%, 89.85%, 88.83% and 82.53% in mCov, mWCov, mPerc90, and mRec90, respectively. In siliques detection, PST-PG obtains RMSE of 21.09 when  $\text{IoU} > 75\%$  and 25.87 when  $\text{IoU} > 90\%$ .

In the future, we will use more different types of plants to enrich the dataset and build up a

more robust and general method for plant point cloud analysis. We wish our work could break the paradigm of designing a plant point cloud segmentation network and inspire more thoughts on high precise phenotyping of plants with complicated structures.

## Reference

- Brock, A., Lim, T., Ritchie, J.M. and Weston, N., 2017. FreezeOut: Accelerate Training by Progressively Freezing Layers.
- Carion, N. et al., 2020. End-to-End Object Detection with Transformers, Computer Vision – ECCV 2020: 16th European Conference, Glasgow, UK, August 23–28, 2020, Proceedings, Part I. Springer-Verlag, Glasgow, United Kingdom, pp. 213–229.
- Dutagaci, H., Rasti, P., Galopin, G. and Rousseau, D., 2020. ROSE-X: an annotated data set for evaluation of 3D plant organ segmentation methods. *Plant Methods*, 16(1).
- Elich, C., Engelmann, F., Kontogianni, T. and Leibe, B., 2019. 3D Bird’s-Eye-View Instance Segmentation, Pattern Recognition: 41st DAGM German Conference, DAGM GCPR 2019, Dortmund, Germany, September 10–13, 2019, Proceedings. Springer-Verlag, Dortmund, Germany, pp. 48–61.
- Engelmann, F., Kontogianni, T., Hermans, A. and Leibe, B., 2017. Exploring Spatial Context for 3D Semantic Segmentation of Point Clouds. *Ieee Int Conf Comp V*: 716-724.
- Engelmann, F., Kontogianni, T., Schult, J. and Leibe, B., 2019. Know What Your Neighbors Do: 3D Semantic Segmentation of Point Clouds. *Lect Notes Comput Sc*, 11131: 395-409.
- Fan, L. et al., 2021. Embracing Single Stride 3D Object Detector with Sparse Transformer, pp. arXiv:2112.06375.
- Friedt, W., Snowdon, R., Ordon, F. and Ahlemeyer, J., 2007. Plant breeding: Assessment of genetic diversity in crop plants and its exploitation in breeding. *Progress in Botany* 68, 68: 151-178.
- Fuersattel, P., Plank, C., Maier, A. and Riess, C., 2017. Accurate laser scanner to camera calibration with application to range sensor evaluation. *IPSJ Transactions on Computer Vision and Applications*, 9(1): 21.
- Fursattel, P. et al., 2016. A Comparative Error Analysis of Current Time-of-Flight Sensors. *Ieee T Comput Imag*, 2(1): 27-41.
- Gibbs, J.A. et al., 2020. Active Vision and Surface Reconstruction for 3D Plant Shoot Modelling. *Ieee Acn T Comput Bi*, 17(6): 1907-1917.
- Golbach, F., Kootstra, G., Damjanovic, S., Otten, G. and van de Zedde, R., 2016. Validation of plant part measurements using a 3D reconstruction method suitable for high-throughput seedling phenotyping. *Mach Vision Appl*, 27(5): 663-680.

- Guo, Q.H. et al., 2020a. Application of deep learning in ecological resource research: Theories, methods, and challenges. *Sci China Earth Sci*, 63(10): 1457-1474.
- Guo, Y. et al., 2020b. Deep Learning for 3D Point Clouds: A Survey. *IEEE transactions on pattern analysis and machine intelligence*, PP.
- Han, L., Zheng, T., Xu, L. and Fang, L., 2020. OccuSeg: Occupancy-Aware 3D Instance Segmentation, 2020 IEEE/CVF Conference on Computer Vision and Pattern Recognition (CVPR), pp. 2937-2946.
- Han, X., Dong, Z. and Yang, B.S., 2021. A point-based deep learning network for semantic segmentation of MLS point clouds. *Isprs Journal of Photogrammetry and Remote Sensing*, 175: 199-214.
- Hua, B.S., Tran, M.K. and Yeung, S.K., 2018. Pointwise Convolutional Neural Networks. 2018 Ieee/Cvf Conference on Computer Vision and Pattern Recognition (Cvpr): 984-993.
- Huang, J. and You, S.Y., 2016. Point Cloud Labeling using 3D Convolutional Neural Network. *Int C Patt Recog*: 2670-2675.
- Huang, Q.G., Wang, W.Y. and Neumann, U., 2018. Recurrent Slice Networks for 3D Segmentation of Point Clouds. 2018 Ieee/Cvf Conference on Computer Vision and Pattern Recognition (Cvpr): 2626-2635.
- Jiang, L. et al., 2020. PointGroup: Dual-Set Point Grouping for 3D Instance Segmentation, IEEE/CVF Conference on Computer Vision and Pattern Recognition (CVPR). IEEE Conference on Computer Vision and Pattern Recognition, Electr Network, pp. 4866-4875.
- Jin, S.C. et al., 2020a. Separating the Structural Components of Maize for Field Phenotyping Using Terrestrial LiDAR Data and Deep Convolutional Neural Networks. *Ieee T Geosci Remote*, 58(4): 2644-2658.
- Jin, S.C., Sun, Y.J., Zhao, X.Q., Hu, T.Y. and Guo, Q.H., 2020b. A Point-Based Fully Convolutional Neural Network for Airborne LiDAR Ground Point Filtering in Forested Environments. *Ieee J-Stars*, 13: 3958-3974.
- Lahoud, J., Ghanem, B., Pollefeys, M. and Oswald, M.R., 2019. 3D Instance Segmentation via Multi-Task Metric Learning. *Ieee I Conf Comp Vis*: 9255-9265.
- Lang, A.H. et al., 2019. PointPillars: Fast Encoders for Object Detection from Point Clouds. *Proc Cvpr Ieee*: 12689-12697.
- Li, D., Shi, G., Kong, W., Wang, S. and Chen, Y., 2020. A Leaf Segmentation and Phenotypic Feature Extraction Framework for Multiview Stereo Plant Point Clouds. *Ieee J-Stars*, 13: 2321-2336.
- Li, D.W. et al., 2022. PlantNet: A dual-function point cloud segmentation network for multiple plant species. *Isprs Journal of Photogrammetry and Remote Sensing*, 184: 243-263.
- Li, S.H. et al., 2017. Estimating Leaf Area Density of Individual Trees Using the Point Cloud Segmentation of Terrestrial LiDAR Data and a Voxel-Based Model. *Remote Sensing*, 9(11).
- Li, Y.Y. et al., 2013. Analyzing Growing Plants from 4D Point Cloud Data. *Acm Transactions on Graphics*, 32(6).



- Liu, S., Jia, J.Y., Fidler, S. and Urtasun, R., 2017. SGN: Sequential Grouping Networks for Instance Segmentation. 2017 Ieee International Conference on Computer Vision (Iccv): 3516-3524.
- Liu, Z. et al., 2021. Swin Transformer: Hierarchical Vision Transformer using Shifted Windows, 2021 IEEE/CVF International Conference on Computer Vision (ICCV), pp. 9992-10002.
- Mo, K.C. et al., 2019. PartNet: A Large-scale Benchmark for Fine-grained and Hierarchical Part-level 3D Object Understanding. Proc Cvpr Ieee: 909-918.
- Ni, X.P., Li, C.Y., Jiang, H.Y. and Takeda, F., 2021. Three-dimensional photogrammetry with deep learning instance segmentation to extract berry fruit harvestability traits. Isprs Journal of Photogrammetry and Remote Sensing, 171: 297-309.
- Oleksy, A., Zajac, T., Klimek-Kopyra, A., Pustkowiak, H. and Jankowski, K., 2018. RELATIVE SILIQUES POSITION IN A CROP LAYER AS AN INDICATOR OF YIELD AND QUALITY IN WINTER RAPE. Pakistan Journal of Agricultural Sciences, 55(4): 727-738.
- Paulus, S., Schumann, H., Kuhlmann, H. and Leon, J., 2014. High-precision laser scanning system for capturing 3D plant architecture and analysing growth of cereal plants. Biosyst. Eng., 121: 1-11.
- Pham, Q.H., Nguyen, D.T., Hua, B.S., Roig, G. and Yeung, S.K., 2019. JSIS3D: Joint Semantic-Instance Segmentation of 3D Point Clouds with Multi-Task Pointwise Networks and Multi-Value Conditional Random Fields. Proc Cvpr Ieee: 8819-8828.
- Qi, C.R., Su, H., Mo, K.C., Guibas, L.J. and Ieee, 2017a. PointNet: Deep Learning on Point Sets for 3D Classification and Segmentation, 30th IEEE/CVF Conference on Computer Vision and Pattern Recognition (CVPR). IEEE Conference on Computer Vision and Pattern Recognition, Honolulu, HI, pp. 77-85.
- Qi, C.R., Yi, L., Su, H. and Guibas, L.J., 2017b. PointNet plus plus : Deep Hierarchical Feature Learning on Point Sets in a Metric Space, 31st Annual Conference on Neural Information Processing Systems (NIPS). Advances in Neural Information Processing Systems, Long Beach, CA.
- Rauscher, G., Dube, D. and Zell, A., 2016. A Comparison of 3D Sensors for Wheeled Mobile Robots. Adv Intell Syst, 302: 29-41.
- Ren, M.Y. and Zemel, R.S., 2017. End-to-End Instance Segmentation with Recurrent Attention. 30th Ieee Conference on Computer Vision and Pattern Recognition (Cvpr 2017): 293-301.
- Rethage, D., Wald, J., Sturm, J., Navab, N. and Tombari, F., 2018. Fully-Convolutional Point Networks for Large-Scale Point Clouds. Computer Vision - Eccv 2018, Pt Iv, 11208: 625-640.
- Sindagi, V.A., Zhou, Y. and Tuzel, C., 2019. MVX-Net: Multimodal VoxelNet for 3D Object Detection. Ieee Int Conf Robot: 7276-7282.
- Sodhi, P., Vijayarangan, S. and Wettergreen, D., 2017. In-field Segmentation and Identification of Plant Structures using 3D Imaging. Ieee Int C Int Robot: 5180-5187.
- Tanksley, S.D., 2004. The genetic, developmental, and molecular bases of fruit size and shape variation in tomato. Plant Cell, 16: S181-S189.

- Thomas, H. et al., 2019. KPConv: Flexible and Deformable Convolution for Point Clouds. *Ieee I Conf Comp Vis*: 6420-6429.
- Tran, D.T. et al., 2017. Population Modeling Approach to Optimize Crop Harvest Strategy. The Case of Field Tomato. *Front. Plant Sci.*, 8.
- Turgut, K., Dutagaci, H., Galopin, G. and Rousseau, D., 2022. Segmentation of structural parts of rosebush plants with 3D point-based deep learning methods. *Plant Methods*, 18(1).
- Vo, A.V., Linh, T.H., Laefer, D.F. and Bertolotto, M., 2015. Octree-based region growing for point cloud segmentation. *Isprs Journal of Photogrammetry and Remote Sensing*, 104: 88-100.
- Wahabzada, M., Paulus, S., Kersting, K. and Mahlein, A.K., 2015. Automated interpretation of 3D laserscanned point clouds for plant organ segmentation. *BMC Bioinformatics*, 16: 11.
- Wang, C.L. et al., 2016. Influence of leaf and silique photosynthesis on seeds yield and seeds oil quality of oilseed rape (*Brassica napus* L.). *Eur. J. Agron.*, 74: 112-118.
- Wang, W.Y., Yu, R., Huang, Q.G. and Neumann, U., 2018. SGPN: Similarity Group Proposal Network for 3D Point Cloud Instance Segmentation. 2018 *Ieee/Cvf Conference on Computer Vision and Pattern Recognition (Cvpr)*: 2569-2578.
- Wang, X.L., Liu, S., Shen, X.Y., Shen, C.H. and Jia, J.Y., 2019a. Associatively Segmenting Instances and Semantics in Point Clouds. *Proc Cvpr Ieee*: 4091-4100.
- Wang, Y. et al., 2019b. Dynamic Graph CNN for Learning on Point Clouds. *Acm Transactions on Graphics*, 38(5).
- Wolko, J., Dobrzycka, A., Bocianowski, J. and Bartkowiak-Broda, I., 2019. Estimation of heterosis for yield-related traits for single cross and three-way cross hybrids of oilseed rape (*Brassica napus* L.). *Euphytica*, 215(10).
- Xi, Z.X., Hopkinson, C., Rood, S.B. and Peddle, D.R., 2020. See the forest and the trees: Effective machine and deep learning algorithms for wood filtering and tree species classification from terrestrial laser scanning. *Isprs Journal of Photogrammetry and Remote Sensing*, 168: 1-16.
- Xiang, L.R., Bao, Y., Tang, L., Ortiz, D. and Salas-Fernandez, M.G., 2019. Automated morphological traits extraction for sorghum plants via 3D point cloud data analysis. *Computers and Electronics in Agriculture*, 162: 951-961.
- Xu, M.T., Ding, R.Y., Zhao, H.S. and Qi, X.J., 2021. PAConv: Position Adaptive Convolution with Dynamic Kernel Assembling on Point Clouds. 2021 *Ieee/Cvf Conference on Computer Vision and Pattern Recognition, Cvpr 2021*: 3172-3181.
- Yang, J.C. et al., 2019. Modeling Point Clouds with Self-Attention and Gumbel Subset Sampling. *Proc Cvpr Ieee*: 3318-3327.
- Ye, X.Q., Li, J.M., Huang, H.X., Du, L. and Zhang, X.L., 2018. 3D Recurrent Neural Networks with Context Fusion for Point Cloud Semantic Segmentation. *Computer Vision - Eccv 2018, Pt Vii*, 11211: 415-430.
- Zermas, D., Morellas, V., Mulla, D. and Papanikolopoulos, N., 2017. Estimating the Leaf Area Index of Crops Through the Evaluation of 3D Models. *Ieee Int C Int Robot*: 6155-6162.
- Zhou, Y. et al., 2019. End-to-End Multi-View Fusion for 3D Object Detection in LiDAR Point

Clouds. ArXiv, abs/1910.06528.

Zhou, Y. and Tuzel, O., 2018. VoxelNet: End-to-End Learning for Point Cloud Based 3D Object Detection. 2018 Ieee/Cvf Conference on Computer Vision and Pattern Recognition (Cvpr): 4490-4499.

Zhuo, W., Salzmann, M., He, X.M. and Liu, M.M., 2017. Indoor Scene Parsing with Instance Segmentation, Semantic Labeling and Support Relationship Inference. 30th Ieee Conference on Computer Vision and Pattern Recognition (Cvpr 2017): 6269-6275.